Time Delays for the Giant Quadruple Lensed Quasar SDSS J1004+4112: Prospects for Determining the Density Profile of the Lensing Cluster

Yozo KAWANO

Department of Physics and Astrophysics, Nagoya University, Chikusa-ku, Nagoya 464-8062.

kawano@a.phys.nagoya-u.ac.jp

and

Masamune OGURI

Department of Astrophysical Sciences, Princeton University, Princeton, NJ 08544, USA.

oguri@astro.princeton.edu

Abstract

We investigate the dependence of the time delays for the large-separation gravitationally lensed quasar SDSS J1004+4112 on the inner mass profile of the lensing cluster. Adopting the mass model whose innermost density profile is parameterized as $\rho \propto r^{-\alpha}$, we derive a series of mass models which can fit observational data and then compute the probability distribution functions of time delays. We find that larger α has longer time delays, longer tails at the higher end of the probability distribution, and larger model uncertainties. The ratios of time delays slightly depend on the slope α. Among others, time delays between images C and A (or B) have little dependence on the inner slope, particularly when the time delays are short. The dependence of time delays on α is well fitted by a linear form, which reflects well-known degeneracy between the mass profile and time delays. We perform a Monte-Carlo simulation to illustrate how well the inner slope can be constrained from measurements of time delays. We find that measurements of more than one time delays result in reasonably tight constraints on the inner slope ($\sigma_\alpha \lesssim 0.25$), while only one time delay cannot determine the inner slope very well. Our result indicates that time delays indeed serve as a powerful tool to determine the mass profile, despite the complexity of the lensing cluster.

Key words: cosmology: theory — galaxies: halos — galaxies: clusters: general — dark matter — galaxies: quasars: individual (SDSS J1004+4112)— gravitational lensing

1. Introduction

Recent high-resolution N-body simulations in the Cold Dark Matter (CDM) universe have suggested that dark matter halos are described by a universal mass profile (Navarro et al. 1996, 1997, hereafter NFW). Higher-resolution simulations have revealed that the innermost region may have steeper inner slopes than originally suggested and may not be universal (Fukushige, Makino 1997, 2001, 2003; Moore et al. 1999; Ghigna et al. 2000; Jing, Suto 2000; Power et al. 2003; Fukushige et al. 2004; Hayashi et al. 2004; Diemand et al. 2004; Tasitsiomi et al. 2004; Reed et al. 2005). While the accurate value of the inner slope and the universality remain controversial, the existence of deep potential well at the center of dark matter halos in the CDM model appears quite robust. Here the important fact is that the inner profile of dark halos is extremely sensitive to nature of dark matter: For instance, if one introduces self-interacting cross sections of dark matter particles, the central density profile becomes much shallower than expected in the standard CDM universe (Spergel, Steinhardt 2000). Therefore it serves as a powerful test of collisionless CDM paradigm. Such observational studies to constrain parameters of the density profile have been conducted. For instance, assuming the hydrostatic equilibrium the mass profile of a dark matter halo can be evaluated from the gas density and the temperature profiles of intra-cluster medium (e.g., Sato et al. 2000); weak lensing reconstruction can reproduce the mass profile of a cluster from ellipticities of galaxies behind the cluster (Kaiser, Squire 1993; Schneider 2005). In particular, rotation curve observations of dark-matter-dominated dwarf and low surface brightness disk galaxies have indicated that they favor mass profiles with a flat density core, being inconsistent with the NFW profile (Salucci, Burkert 2000; de Blok, Bosma 2002; Swaters et al. 2003; Gentile et al. 2004). However, this apparent discrepancy might be because of bias in gas rotation speed (Hayashi et al. 2004) or the destruction of central cusps by the formation of a primordial bar (Weinberg, Katz 2002). Thus, investigations of the halo density profiles in different systems has been one of the most essential issues.

Among others, one of the most promising methods to test the NFW profile would be strong lensing by clusters of galaxies. Gravitational lensing is unique in the sense that it allows one to detect the mass distribution *directly* (Refsdal 1964; Bourassa et al. 1973, 1975, 1976; Wambsganss, Paczyński 1994; Keeton et al. 1997; Mao, Schneider 1998; Chiba 2002; Kawano et al. 2004; Kochanek, Dalal 2004). In particular, strong lensing by clusters is a indispensable tool to probe the innermost region of dark matter halos, since most baryons in clusters remain hot and diffuse and therefore the density profile of clusters can be well approximated by that of dark halos seen in N-body simulations. For instance, giant arcs of background galaxies with different redshifts (Einstein radii) can strongly constrain the mass profiles of clusters (Broadhurst et al. 2005). This is because the mass inside the Einstein ring with radius $r_{\rm E}$ at which arcs build up is proportional to $r_{\rm E}^2$ and thus multiple arcs with different redshifts

determine the masses within the different radii, equivalently the mass slope. Multiply imaged quasars due to clusters of galaxies offer another direct probe of the mass profiles of lensing clusters. Indeed, they have several advantages over giant arcs. First, for lensed quasar systems it is easier to correct selection bias of lensing clusters (i.e., difference between lensed and unlensed cluster populations; see e.g., Hennawi et al. 2005) because of well-known source population of quasars. Second, we can measure time delays for lensed quasars, which serves as additional strong constraints on the mass distribution.

Recently, the first example of such quasar-cluster lens system, SDSS J1004+4112, has been discovered (Inada et al. 2003; Oguri et al. 2004) in the Sloan Digital Sky Survey (SDSS; York et al. 2000). It has an unusual separation of ~ 15 arcsec, which is more than twice larger than the second largest lens Q 0957+561 (Walsh et al. 1979). The quasar and lensing cluster have redshifts of 1.74 and 0.68, respectively. The central region of the lens cluster is dominated by the brightest cluster galaxy. The fifth image of the lensed quasar, which constrains inner mass distribution of the the brightest cluster galaxy strongly, was discovered by Inada et al. (2005).

How did the lens system SDSS J1004+4112 constrain the inner mass distribution of the dark matter halo? Oguri et al. (2004) modeled the lens with singular isothermal ellipsoid (SIED) plus NFW, and found that the image configurations and fluxes are reproduced well. More generally, Williams, Saha (2004) adopted a free-form mass reconstruction technique (Saha, Williams 1997) and pointed out that the quadruple images alone do not give useful constraints on the inner slope of the dark matter halo. Therefore, we need additional information: One such information comes from arcs of background galaxies which have already observed by Sharon et al. (2005). Arcs at several radii (redshifts) can constrain the inner slope since we can estimate the mass inside a arc from the the arc position and shape. Another information, which is unique for lensed quasar systems, is time delays between each images. It has been shown that the Hubble constant and the slope of the density profile are both sensitive to time delays (Wambsganss, Paczyński 1994; Oguri et al. 2002; Wucknitz 2002; Kochanek 2002; Oguri, Kawano 2003; Kochanek et al. 2005), therefore by assuming the value of the global Hubble constant, which is now determined with better than 10% accuracy (Freedman et al. 2001; Spergel et al. 2003), we will be able to obtain useful information on the mass profile. The image configuration of the system is very similar to that of PG 1115+080 (Weymann et al. 1980), however the separations are scaled by a factor of ~ 8 and hence the time delays are longer by a factor of $\sim 8^2$, which means that the shortest and longest time delays would be ~ 10 days and ~ 1000 days, respectively. However, the complexity of the cluster mass distribution makes the possible range of time delays quite large (Oguri et al. 2004; Williams, Saha 2004). Therefore it is not obvious whether time delays can really give meaningful constraints on the inner profile of the dark matter halo. In this paper, we investigate in detail the capability of measuring time delays and constraining the inner mass slope of the cluster.

This paper is organized as follows. In section 2 we describe our model to predict time delays for SDSS J1004+4112. Section 3 gives the predictions of time delays and the probability distributions of them. Then, a likelihood analysis is performed in section 4 to see how time delays constrain the radial slope of the cluster mass. We finally discuss the results and give conclusions in section 5.

2. Lens Mass Modeling

A source at $\mathbf{y}$ and an i-th image at $\mathbf{x}_i$ are related through the lens equation

$$\mathbf{y} = \mathbf{x}_i - \nabla \psi(\mathbf{x}_i), \tag{1}$$

where $\psi(\mathbf{x}_i)$ is the projected lens potential (Schneider et al. 1992). The vectors are defined on the sky (lens and source planes). The lens potential can be expressed as

$$\psi(\mathbf{x}) = \frac{1}{\pi} \int d^2 x' \kappa(\mathbf{x}') \ln |\mathbf{x} - \mathbf{x}'|, \tag{2}$$

where $\kappa(\mathbf{x}_i)$ is the dimensionless surface mass density, so called convergence. More specifically, the convergence is proportional to the surface mass density $\Sigma(\mathbf{x})$ as

$$\kappa(\mathbf{x}) = \frac{\Sigma(\mathbf{x})}{\Sigma_{\rm cr}}, \tag{3}$$

where $\Sigma_{\rm cr}$ is the critical surface mass density defined by

$$\Sigma_{\rm cr} \equiv \frac{c^2}{4\pi G} \frac{D_{\rm s}}{D_{\rm d} D_{\rm ds}}, \tag{4}$$

with $D_{\rm d}$, $D_{\rm s}$ and $D_{\rm ds}$ being the angular diameter distances to the lens, to the source, and from the lens to the source, respectively. The gravitational lenses magnify the flux of i-th image by the factor of $\mu(\mathbf{x}_i)$:

$$\mu(\mathbf{x}_i) = \left| \det \left(\frac{\partial \mathbf{y}}{\partial \mathbf{x}} \right)_{\mathbf{x} = \mathbf{x}_i} \right|^{-1}. \tag{5}$$

The relative time delay between i-th and j-th images is then calculated from

$$\Delta t_{ij} = \frac{1 + z_{\rm d}}{c} \frac{D_{\rm d} D_{\rm s}}{D_{\rm ds}} \left[\frac{1}{2} \Delta \mathbf{x}_i^2 - \frac{1}{2} \Delta \mathbf{x}_j^2 - \psi(\mathbf{x}_i) + \psi(\mathbf{x}_j) \right], \tag{6}$$

where $\Delta \mathbf{x}_i = \mathbf{x}_i - \mathbf{y}$. Provided that one knows redshifts of the source and the lens, position and flux of the source, and mass distribution (potential) of the lens as well as the cosmological parameters, one can calculate observable quantities such as the number of images, image positions, fluxes, and time delays. Turning the problem around, by measuring the redshifts, image positions and fluxes, and relative time delays, one can constrain the mass distribution of the lens.

In this paper, we consider a specific quadruple lens system, SDSS J1004+4112, the first quasar multiply lensed by a central part of a massive cluster. There has been a variety of studies to investigate the structures of the lensing cluster. Oguri et al. (2004) firstly performed

4

an enormous amount of modeling of the system with realistic two-component models. Provided that the galaxy has a SIED and the cluster has an elliptical version of NFW profile with an external shear, respectively, they concluded that: 1) there is a offset between the centers of the brightest galaxy and the cluster; 2) a wide range of the models can reproduce the position angle of the galaxy well; 3) the elongation of modeled cluster are also similar to the observed distribution of cluster galaxies; 4) they found a large tidal shear (~ 0.2) which suggests significant substructure in the cluster; 5) there is an enormous uncertainty in the predicted time delays between the quasar images, which indicates that measuring the delays would greatly improve constraints on the models; 6) measuring the time delay between image A and B would determine the temporal ordering such as C-B-A-D and give an expected value of the delay between image C and D; 7) the scale length of the dark matter of the cluster would be $r_\mathrm{s} \geq 30''$ from predicted relation between r_s and the lensing strength (see below for the definition of r_s). On the other hand, Williams, Saha (2004) presented free-form reconstructions of the lens with constraints of the image positions and physical conditions. The modeling gave some important results: 1) the projected cluster mass profile is consistent with being $r^{-0.3...-0.5}$, which can be fitted with either the NFW or a flat core model; 2) the residual mass maps created by subtracting the circularly averaged surface mass density shows the significant substructures; 3) D-A-B-C time ordering results in shift $\simeq 3''$ of the lens center and then tends to allow a lot of models with spurious extra images — the time ordering seems very unlikely; 4) a measurement of time delay between A and B would serve as a test of the shallow mass profile. Inada et al. (2005) discovered the fifth central image and tested the ability of the image to constrain the mass profile of the bright cluster galaxy. They assumed a power-law density profile $\rho(r) \propto r^{-\gamma}$ which potential was set to have an elliptical symmetry for the galaxy and concluded that the central bright cluster galaxy cannot have steeper mass profile than isothermal ($\gamma \leq 2$) to reproduce the flux. Sharon et al. (2005) discovered multiply imaged arcs of three galaxies at high redshifts. Their different redshifts correspond to different radii of Einstein rings because of different critical surface mass densities. Since multiply imaged arcs constrain the mass inside the arcs, they obtained the average projected surface mass slope consistent with NFW (~ -0.5) from their simple (preliminary) one-component modeling of the dark matter halo. We note that the lensing probability can constrain the mass profile as well (Oguri et al. 2004; Oguri, Keeton 2004), but the constraint degenerates strongly with cosmological parameters.

Following Oguri et al. (2004), in this paper we consider the two-component model that consists of the brightest cluster galaxy and dark matter components. However, an important extension of the model in this paper is that we allow various inner slopes of dark matter components to study their effects on time delays. More specifically, we model the brightest cluster galaxy, which Oguri et al. (2004) called G1, as an SIED

$$\kappa(x,y) = \frac{b}{2\xi}, \tag{7}$$

Table 1. Constraints on Mass Models

Object	x (arcsec)[*]	y (arcsec) [*]	Flux (arbitrary)[†]	P.A. (deg) [‡]
A	0.000 ± 0.001	0.000 ± 0.001	1.000 ± 0.200	...
B	-1.317 ± 0.002	3.532 ± 0.002	0.732 ± 0.146	...
C	11.039 ± 0.002	-4.492 ± 0.002	0.346 ± 0.069	...
D	8.399 ± 0.004	9.707 ± 0.004	0.207 ± 0.041	...
G1	7.114 ± 0.030	4.409 ± 0.030	...	-19.9 ± 20.0

[*] The positive directions of x and y are defined by West and North, respectively.

[†] Errors are broadened to 20% to account for possible systematic effects.

[‡] Degree measured east of north.

where $\xi = \sqrt{x^2 + y^2/q^2}$, b is a characteristic deflection angle which is related to the velocity dispersion σ_v of the galaxy by

$$b = 4\pi \frac{D_{\mathrm{ds}}}{D_{\mathrm{s}}} \left(\frac{\sigma_v}{c}\right)^2, \tag{8}$$

and q is an axis ratio of the projected mass distribution. The separation of the lensed images is so large that the small deviation from the isothermal profile have little effect on predictions of the time delays. The cluster of galaxies is modeled as a generalized NFW profile (GNFW)

$$\rho = \frac{\rho_{\mathrm{s}}}{(\sqrt{\xi^2 + z^2}/r_{\mathrm{s}})^{\alpha}(1 + \sqrt{\xi^2 + z^2}/r_{\mathrm{s}})^{3-\alpha}}, \tag{9}$$

where r_{s} is a scale length, ρ_{s} is a characteristic density (computed from the scale length r_{s} and the virial mass M_{vir}), and α is an inner density slope ($\rho \propto r^{-\alpha}$). The surface mass density of this GNFW profile is obtained by integrating equation (9) over z. As done by Oguri et al. (2004), an external shear is added in order to approximately include the effects of possible complex structure in the outer region of the cluster.

In order to exclude unphysical situations, we assume that b is smaller than 2.25 arcsec because any galaxies should have the velocity dispersion smaller than $400 \mathrm{kms}^{-1}$. The inner mass slope α is restricted to 0.5, 0.75, 1.0, 1.25, 1.5 mainly because of the computational limitation. We note that NFW originally proposed $\alpha = 1$ universal model and recent N-body simulations have suggested that α is approximately between 1 and 1.5. We fix $r_{\mathrm{s}} = 40''$, because Oguri et al. (2004) concluded that $r_{\mathrm{s}} \geq 30''$, which is much larger than the values of the distances between the lens center and the images. In an inner region ($r \ll r_{\mathrm{s}}$), profiles with different scale lengths are not much different from each other while varying α has much larger effects. This is clearly demonstrated in Figure 1, where we show the predicted time delays of $r_{\mathrm{s}} = 40''$, $60''$ (each point in the Figure corresponds to one of statistically acceptable models; see below for more details). This figure implies that the dependence on the scale length is not important in the case of SDSS J1004+4112, as long as the scale length is reasonably large, $r_{\mathrm{s}} \geq 30''$. Therefore, the number of the model parameters for each α is 15: the position, mass, ellipticity, and position angle of the central galaxy G1; the position, mass, ellipticity, and position angle of the cluster (GNFW);
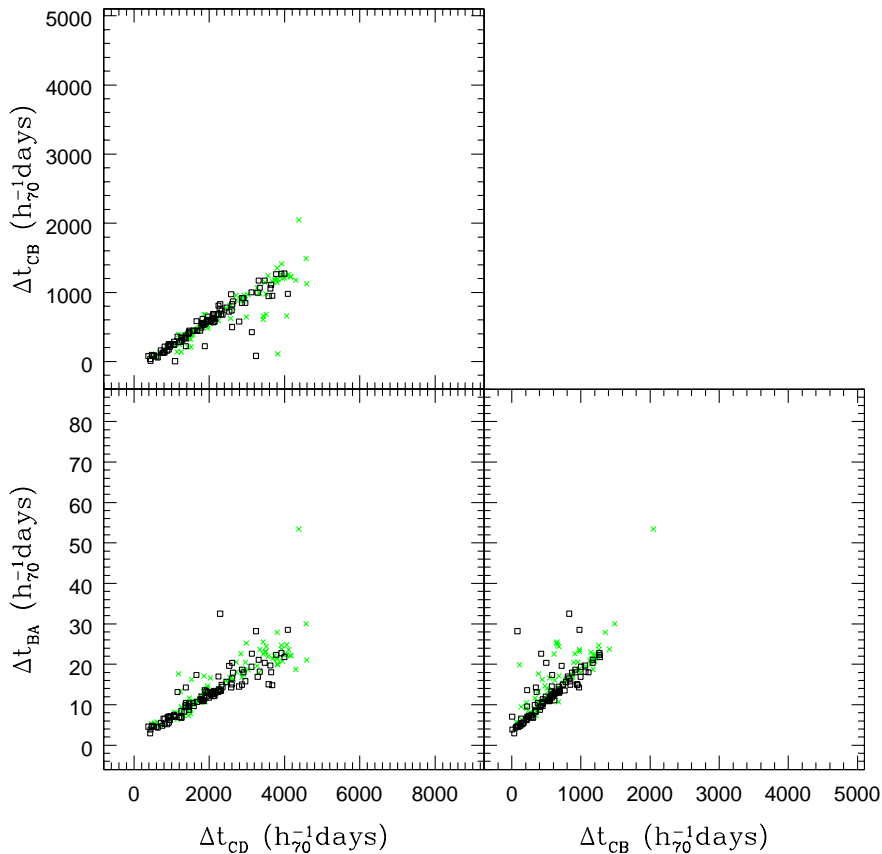
Fig. 1. Predictions of the three time delays for models with different scale length. We fix the inner density slope to $\alpha = 1$. Green crosses show predictions for $r_{\rm s} = 40''$ and black squares denote those for $r_{\rm s} = 60''$.

the amplitude and position angle of the external shear; the position and flux of the source.

For observed positions and fluxes of the quasar and the central galaxy, we use the data of Inada et al. (2005), which is summarized in Table 1. For the purpose of investigating relative time delays between the large-separation images, information of the fifth image is not included in our calculation, because its position and flux are supposed to be governed mainly by the detailed mass distribution of the bright cluster galaxy G1 rather than that of the dark matter halo. Actually, we assume the galaxy to have an isothermal mass profile and then our profile has passed the test of Inada et al. (2005). In addition to image positions and fluxes of the the quasar and the galaxy, the data of a position angle of the galaxy ($\theta_g \sim -19°.9 \pm 20°.0$) is used to constrain our model since the projected mass and light are generally aligned to each other (Keeton et al. 1998). As a result, there are 15 constraints on mass models.

Since the numbers of the model parameters and the observables are equal to each other, it is expected that a wide range of parameter space can fit the data (e.g., Keeton, Winn 2003; Oguri et al. 2004). Following their work, we derive a series of acceptable models as follows. First, we start from a random starting point in the parameter space. We put the parameters initially
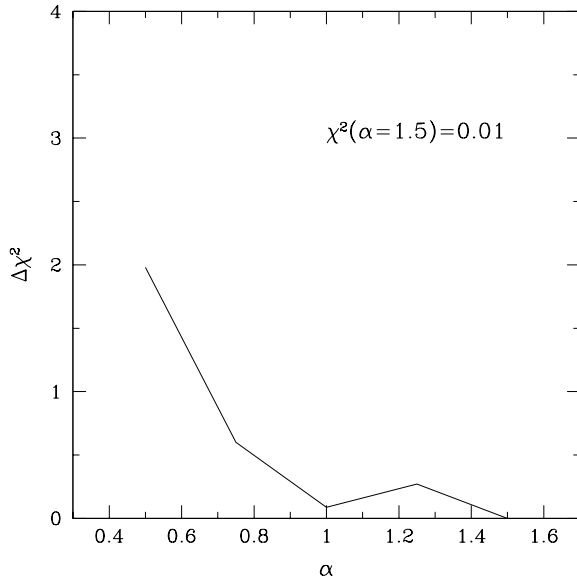
Fig. 2. The $\Delta\chi^2$ distribution as a function of the inner slope α. The minimum χ^2 was achieved at $\alpha = 1.5$, and the value was $\chi^2 = 0.01$.

on the range $0'' < b < 2''.25$, $6''.964 \leq x(\mathrm{G1}) \leq 7''.264$, $4''.259 \leq y(\mathrm{G1}) \leq 4''.559$, $0 \leq e_\mathrm{g} \leq 0.9$, $-59°.9 \leq \theta_\mathrm{g} \leq 20°.1$, $0 < \kappa_\mathrm{s} = \rho_\mathrm{s} r_s / \Sigma_\mathrm{cr} \leq 1.5$, $0 \leq e_\mathrm{c} \leq 0.9$, $-90°.0 \leq \theta_\mathrm{c} \leq 90°.0$, $0 \leq \gamma \leq 0.8$, $-90°.0 \leq \theta_\gamma \leq 90°.0$, where e_g is the ellipticity of the galaxy, e_c and θ_c are the ellipticity and its position angle of the cluster, and γ and θ_γ are the amplitude and its position angle of the external shear, respectively. We then perform a χ^2 minimization and find a local minimum in the χ^2 surface. We adopt *lensmodel* package (Keeton 2001) to solve the lens equation and to perform χ^2 minimization. If the χ^2 of the minimum is < 11.8, we regard it as an acceptable model, and pick it up[1]. Any model with $b > 2''.25$ or unusually large ellipticities $e = 1 - q > 0.9$ is excluded so as not to include unphysical models in our analysis. Because of the result 3) of Williams, Saha (2004) described above, we allow only the models that predict C-B-A-D time ordering. By repeating this process from random numerous starting points, we obtain a group of acceptable models. Most ($> 90\%$) of local minima in the parameter space are excluded because they are not physical or give bad fits statistically. For each α, we determine 100 acceptable models accordingly.

Throughout the paper we adopt a flat lambda-dominated universe with $(\Omega_0, \Omega_\Lambda) = (0.3, 0.7)$, where Ω_0 is the density parameter of matter and Ω_Λ is the dimensionless cosmological constant. However, our predicted time delays can be converted to those in any other cosmologies via equation (6). The Hubble constant in units of 70 km s^{-1} Mpc^{-1} is denoted by h_{70}.

---

[1]   The value of 11.8 represents the 3σ limit in a projected two-dimentional parameter space, when $\chi^2_\mathrm{min} = 0$. We note that the value was also adopted in Oguri et al. 2004.
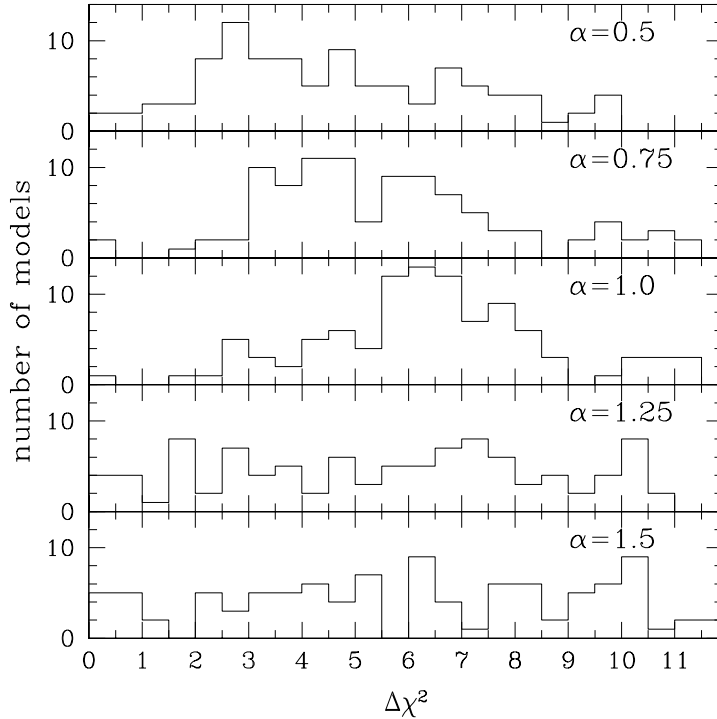
Fig. 3. The $\Delta\chi^2$ distributions of our 100 acceptable models for each α.

3. Predictions of Time Delays

Using the method described in the previous section, we fit the gravitational lens system SDSS J1004+4112 with varying inner mass slopes, $\alpha = 0.5$, 0.75, 1.0, 1.25, 1.5. First, we regard α as a parameter and compute $\Delta\chi^2 \equiv \chi^2 - \chi^2_{\min}$. For each α, the other model parameters are optimized. The result is shown in Figure 2. The minimum χ^2 is very small because the degree of freedom (hereafter DOF) is 0 and therefore the mass model that reproduces the observables perfectly can exist, as is often the case with the analysis of strong lens systems (e.g., Keeton, Winn 2003; Pindor et al. 2005). This confirms earlier claims that only image positions and fluxes cannot constrain the inner mass slope α very well.

Figure 3 shows the $\Delta\chi^2$ of the models for each α. Their distribution have no distinct feature and therefore local minima of χ^2 are expected to exist in a broad range of the parameter space. Thus the predicted time delays should also have a broad range of values. In what follows we consider only local minima and neglect the distributions of χ^2 around local minima, because the differences of time delays between different local minima are typically much larger than the uncertainties of time delays around local minima (see also Keeton, Winn 2003). The time delays that local minima predict are shown in Figure 4 for $\alpha = 0.5$, 1.0, 1.5. As shown in Oguri et al. (2004, for $\alpha = 1.0$), all the two of the time delays, for instance the time delay between A and B, and C and D, are approximately proportional to each other. We find that this is also
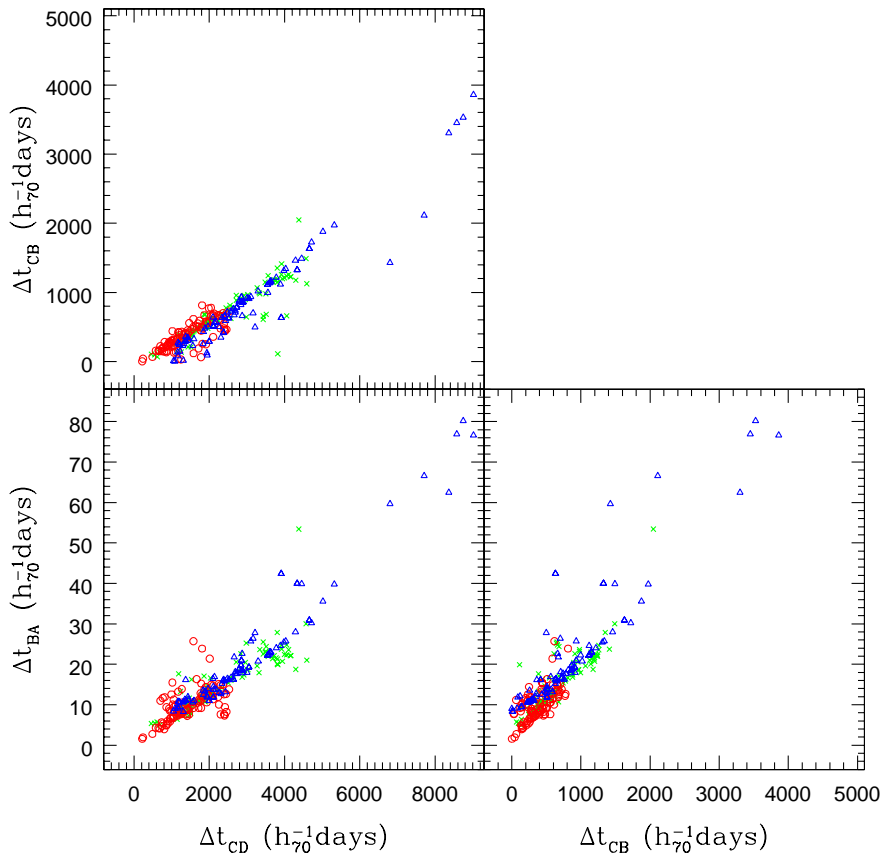
9

Fig. 4. Predictions of the three time delays for different inner slopes: $\alpha = 0.5$ (red circles), 1.0 (green crosses), 1.5 (blue triangles). We show time delay predictions for a group of acceptable models: Each point indicates predicted time delays of one of the models.

the case for $\alpha \neq 1$. However, the dispersion is so large — one short time delay does not always give the other two short time delays. The distribution in longer time delays is sparse relative to that in shorter ones. As increasing α, the distribution shifts to longer time delay space and the dispersion becomes larger. There is different trends in the short time delay edges in the time delay space for different values of α. Thus, the ratios between time delays are expected to vary by the inner mass slope α.

The tendency of increasing time delays with increasing inner slope α may be explained in terms of the famous radial mass index versus the Hubble constant degeneracy (Wambsganss, Paczyński 1994; Oguri et al. 2002; Wucknitz 2002; Kochanek 2002; Oguri, Kawano 2003; Kochanek et al. 2005). Wucknitz (2002) showed that modeling a lens galaxy with observed time delay as having convergence $\kappa \propto r^{\beta-2}$ results in the degeneracy $h_{70} \propto (2-\beta)$. More properly, larger β leads to smaller $h_{70}\Delta t_{ij}$ when all the images exist at similar radii. The inner mass distribution of the GNFW profile is $r^{-\alpha}$, hence its projected mass profile is approximately $\propto r^{-\alpha+1}$ in the case of the GNFW profile. Thus, larger α leads to longer Δt_{ij}
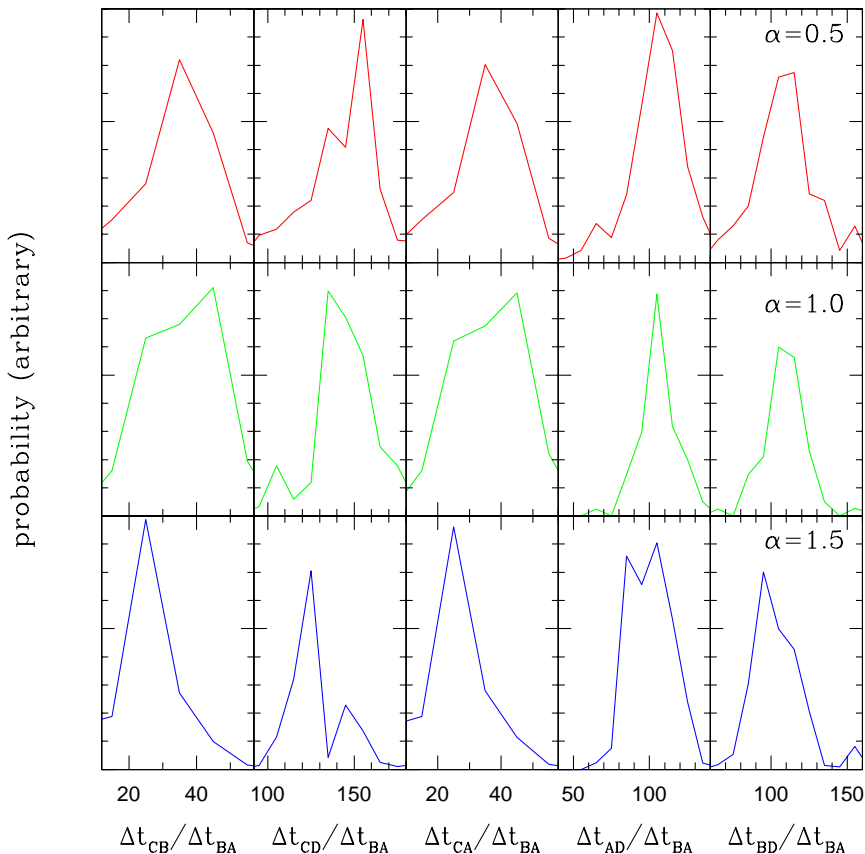
10

Fig. 5. Probability distribution functions of time delay ratios for inner slopes $\alpha = 0.5$ (red lines), 1.0 (green lines), 1.5 (blue lines). Their normalizations are arbitrary.

for the fixed Hubble constant. We confirm that this tendency, at least qualitatively, exists even in SDSS J1004+4112 for which the existence of the central galaxy G1 and substructures in clusters complicates the total mass distribution.

To evaluate distributions of predicted time delays, we construct the probability distribution functions (PDFs) of all the six time delays (Δt_{BA}, Δt_{CB}, Δt_{CD}, Δt_{CA}, Δt_{AD}, Δt_{BD}) and the ratios between them, by summing up all acceptable models with the weight of $\exp[-(\chi^2 - \chi^2_{\mathrm{min}})/2]$. Again, we neglect the distributions of χ^2 around each local minimum, since the predicted time delays does not significantly change around each local minimum and the uncertainties of time delays are similar for different local minima. Because of the fact that width of the valley of the local minimum is not significantly changing, we can exclude the statistical weight. Our choice of the maximum χ^2, 11.8, is not problematic because it corresponds to more than 99% ($\Delta \chi^2 = 11.3$) confidence limit even for DOF $= 3$. They enable one to show that observing the time delays may be able to constrain the mass profile, especially the slope α. The PDFs are constructed as
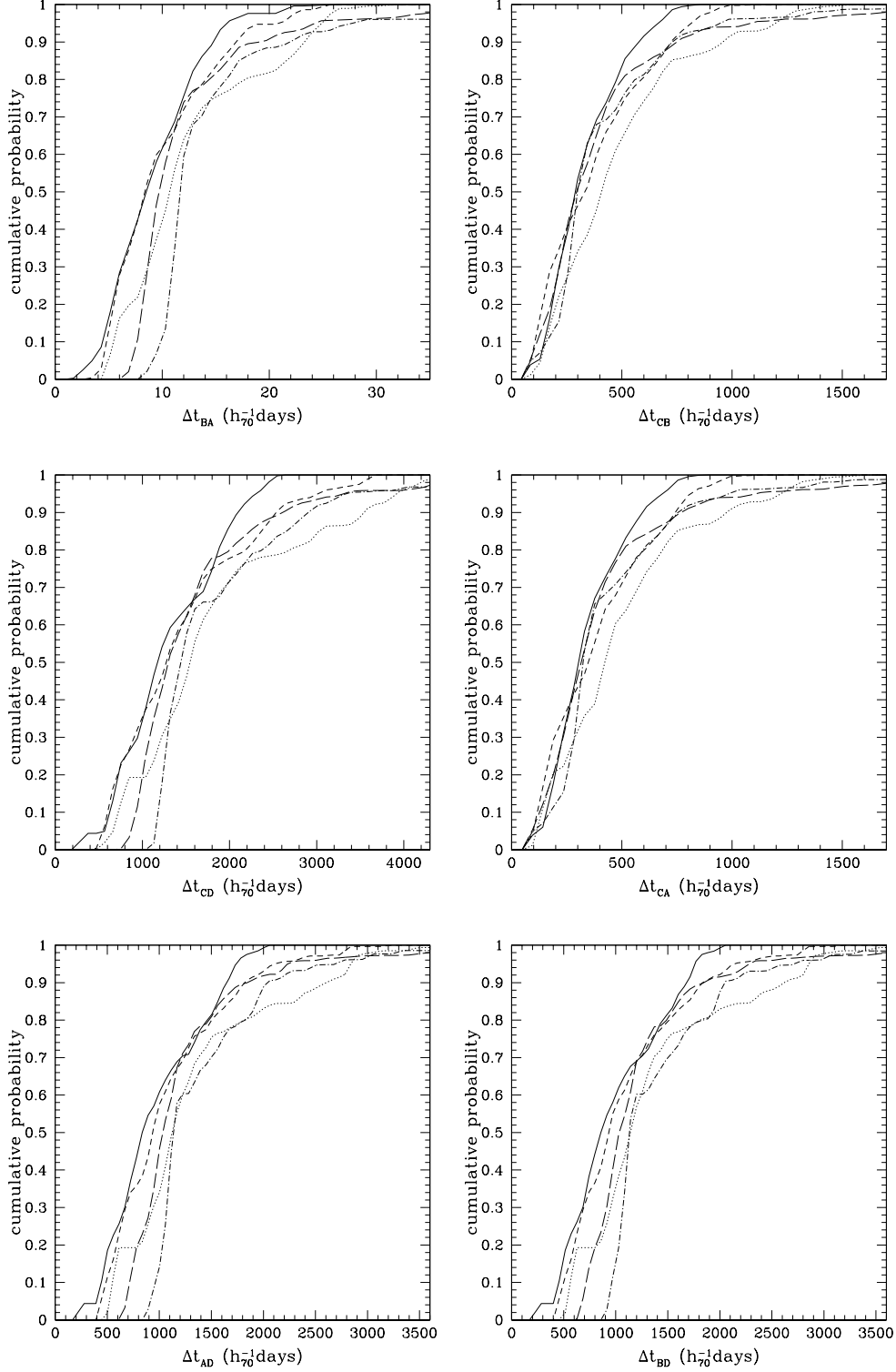
11

Fig. 6. Cumulative probability distribution functions of time delays of any pairs. In each panel, we show the PDFs for different inner slopes: $\alpha = 0.5$ (*solid*), 0.75 (*short dashed*), 1.0 (*dotted*), 1.25 (*long dashed*), and 1.5 (*dot-dashed*).
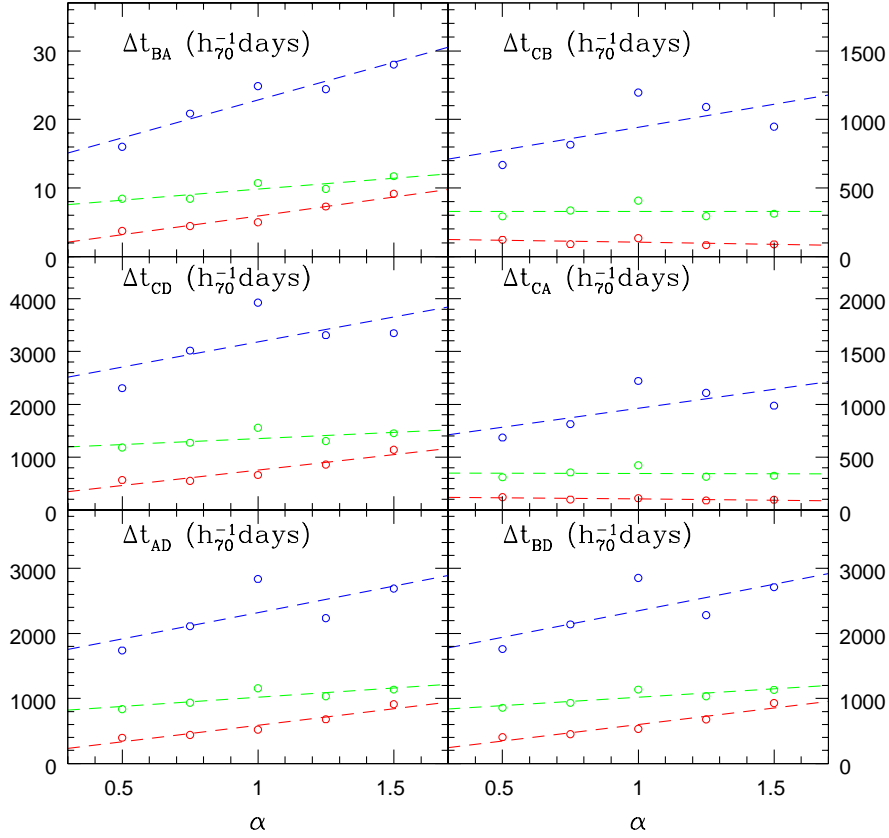
12

Fig. 7. Time delays at which the cumulative probabilities reach 5% (red), 50% (green), and 95% (blue), are plotted as a function of the inner slope α. The dashed line indicates the linear fit (eq. [12]). The fitting parameters are summarized in Table 2.

$$P_{ij}(\Delta t|\alpha) \propto \sum_{k}^{100} \exp\left(-\frac{\chi_k^2 - \chi_{\min}^2}{2}\right)\delta(\Delta t - \Delta t_{ij,k}), \tag{10}$$

where subscript min denotes the minimum χ^2 (for each fixed α). In fact, we divide each time delay into 100 cells, which all have regular intervals, and calculate the PDF on each cell. The PDFs in two and three time delay spaces are defined in the same way. Similarly, the cumulative probability distribution function can also be defined as

$$P_{ij}(<\Delta t|\alpha) = \int_0^{\Delta t} P_{ij}(\Delta t'|\alpha)d(\Delta t'). \tag{11}$$

Before going to the PDFs of time delays themselves, we see the PDFs of time delay ratios in Figure 5. They slightly broaden but clearly reveal the proportionality seen in Figure 4. The PDFs of ratio $\Delta t_{CD}/\Delta t_{BA}$ for $\alpha = 1.0$ is in good agreement with the value 143 ± 16 of Oguri et al. (2004). However, mean values of some ratios are changing significantly with changing α. For example, the ratio $\Delta t_{CD}/\Delta t_{BA}$ for $\alpha = 0.5$ and 1.5 are ~ 155 and ~ 125, respectively. The ratios $\Delta t_{AD}/\Delta t_{BA}$ and $\Delta t_{BD}/\Delta t_{BA}$ depend weakly on the slope — the value of α has relatively

13

Table 2. Fitting Result

Δt_{ij}	$C_1(95\%)$	$C_2(95\%)$	$C_1(50\%)$	$C_2(50\%)$	$C_1(5\%)$	$C_2(5\%)$
Δt_{BA}	11.8	11.0	6.6	3.2	0.4	5.5
Δt_{CB}	609.1	334.3	330.0	-1.7	132.3	-29.1
Δt_{CD}	2232.3	949.1	1125.1	228.6	173.1	582.9
Δt_{CA}	603.7	359.4	350.3	-4.6	126.6	-22.9
Δt_{AD}	1512.0	810.9	739.1	280.6	79.1	510.3
Δt_{BD}	1532.3	818.3	758.6	260.0	89.7	509.1

much effect between image C and the other images. Thus, from the measurements of the time delay between A and B, we can estimate the time delays between A and D, and B and D in good accuracy, regardless of the inner slope α. The dependence of image C on the slope α corresponds the edges we have seen in Figure 4, to some extent. We note that this figure is important to determine the observing strategy of the time delays after measuring the shortest time delay Δt_{BA}. The figure also implies that determining multiple time delays leads to tighter constraints on the inner mass slope α.

Next we see the PDFs of time delays. Figure 6 shows the cumulative probability of all the six time delays. The probability has clear features which we cannot easily see in the time delay space (Figure 4), which are summarized as follows:

1. The models with smaller α have a large fraction of short time delays, and the shorter minimum and maximum time delays. For instance, $\alpha = 0.5$ model has predicted Δt_{BA} of $\sim 1 - 26$ h_{70}^{-1} days, and its cumulative probability reaches 50% at $\Delta t_{\mathrm{BA}} \sim 8$ h_{70}^{-1} days which is nearly equal to the minimum value of $\alpha = 1.5$ model, while $\alpha = 1.5$ model has predicted Δt_{BA} of $\sim 8 - 82$ h_{70}^{-1} days, and its cumulative probability reaches 50% at $\Delta t_{\mathrm{BA}} \sim 11$ h_{70}^{-1} days.

2. The larger α model has a longer tail of the probability distribution and hence the model uncertainties becomes larger with increasing α.

3. For only Δt_{CB} and Δt_{CA} the probability in the short time delay region gives different feature — α dependence cannot be almost seen in a region of the short time delays.

Put another way, increasing α makes the probability distribution to shift to longer time delays and to have longer tails. Thus, in principle the measurement of time delays will constrain an acceptable range of α. However, only one observed time delay, for example Δt_{BA} which is the shortest one and likely to be measured most easily, constrains α weakly, given the large overlap of the PDFs seen in Figure 6. The exception is the observation of very short or long time delay, which gives us the higher or lower limit on the value of α. Because of the third feature, it is supposed that constraint from the time delay between image B and C is weak, if the time delay is relatively short.

As described above, the famous mass-slope versus $h_{70}\Delta t_{ij}$ degeneracy may explain that

larger α models give longer time delays. To test this more explicitly, Figure 7 shows time delays at which the cumulative PDFs reach 5%, 50%, and 95% for different values of the inner slope α. We can fit them with simple linear lines well. Specifically, we fit them as

$$\Delta t_{ij}(P_{ij}(< \Delta t_{ij}|\alpha) = 5\%, \ 50\%, \ 95\%) = (C_1 + C_2\alpha)h_{70}^{-1}\text{days}. \tag{12}$$

We summarize the fitting parameters C_1 and C_2 in Table 2. But the time delays do not exactly obey the linear law of the scaling relation $\propto (\alpha - 1)$. While the discrepancy may reflect the complicated mass distribution of the lensing cluster, we still have the qualitative relationship between the slope of the mass distribution and time delays.

4. Constraints on the Radial Slope of the Cluster Mass

From the discussions in the previous section, it is not obvious how well we can constrain the inner slope α from the measurements of time delays. Thus, in this section we present a Monte-Carlo analysis for this. First, we assume the value of the inner mass slope α and randomly pick up a model from 100 models which are used to construct the PDFs. In other word, we assume that one, two, or three of time delays the model predicts are "observed." The errors of the "observed" time delays are assumed to be 10% Gaussian because most of observed time delays so far have errors of $\sim 10\%$. Then, we calculate the likelihood function

$$\mathcal{L}(\alpha) = \int P_{ij}(\Delta t|\alpha)G(\Delta t_{ij})d(\Delta t_{ij}) \tag{13}$$

for each α. $G(\Delta t_{ij})$ is a Gaussian function

$$G(\Delta t_{ij}) = \frac{1}{\sqrt{2\pi}\sigma_{\Delta t_{ij}}} \exp\left[-\frac{(\Delta t_{ij} - \Delta t_{ij,\text{obs}})^2}{2\sigma_{\Delta t_{ij}}^2}\right], \tag{14}$$

with $\Delta t_{ij,\text{obs}}$ and $\sigma_{\Delta t_{ij}} = 0.1\Delta t_{ij,\text{obs}}$ being the value of randomly generated "observed" time delay and its error, respectively. Hereafter we consider the three situations: 1) only one time delay (Δt_{BA}) is measured, 2) two of three time delays (Δt_{BA}, Δt_{CB}) are measured, and 3) all the three time delays (Δt_{BA}, Δt_{CB}, Δt_{CD}) are measured. For the cases of multiple measurements of time delays, the likelihood becomes multiple-order integral. For each α, we use nine models which are randomly chosen from 100 fitted models. We calculate the integral on each cell in same way as calculating PDFs. Table 3 shows time delays in units of h_{70}^{-1} days, which we adopt to constrain the slope α. For instance, when we assume that three time delays of a model of (1.25-6), we insert $\Delta t_{\text{BA,obs}} = 27.4$, $\Delta t_{\text{CB,obs}} = 1353.4$, $\Delta t_{\text{CD,obs}} = 4567.2$, $\sigma_{\Delta t_{\text{BA}}} = 2.74$, $\sigma_{\Delta t_{\text{CB}}} = 135.34$, $\sigma_{\Delta t_{\text{CD}}} = 456.72$ in units of h_{70}^{-1}days into equation (14), and then from equation (13) we calculate the likelihood function for each α with the PDF constructed in §3.

The results are shown in Figure 8. Each thin and thick solid line show likelihoods from each realization and likelihoods averaged over nine realizations. From only one time delay measurement, one cannot constrain the inner mass profile α significantly, as expected. But by measuring multiple time delays the inner slope can be constrained with good accuracy
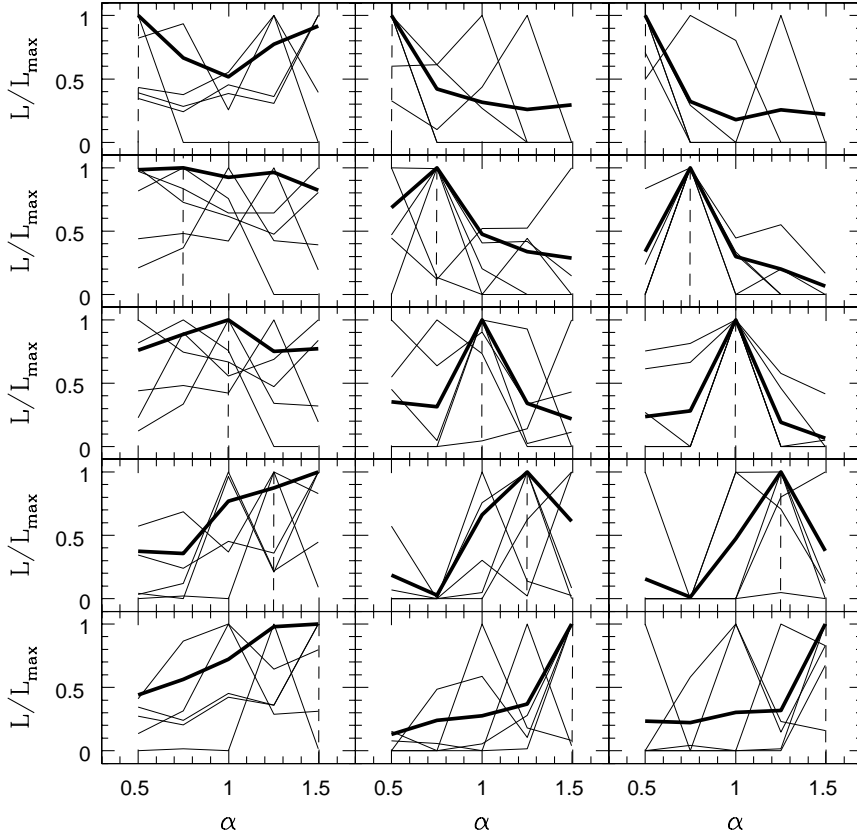
15

Fig. 8. The likelihood function $\mathcal{L}/\mathcal{L}_{\mathrm{max}}$ as a function of the inner slope α. From top to bottom, the input α, denoted by short dashed lines, are 0.5, 0.75, 1.0, 1.25, 1.5, respectively. The numbers of time delays for constraining the slope are one (Δt_{BA}), two (Δt_{BA}, Δt_{CB}), and three (Δt_{BA}, Δt_{CB}, Δt_{CD}) from left to right panels. Thin solid lines show the distributions of $\mathcal{L}/\mathcal{L}_{\mathrm{max}}$ for each realizations (only 5 out of 9 realizations are shown, mainly because of the illustrative reason), and thick solid lines indicate the distributions after averaging over all 9 realizations.

($\sigma_\alpha \lesssim 0.25$). While each time delay, especially Δt_{CB}, gives us little information, the combination of time delays leads us to a true value of the slope. We then conclude that longer time delays in addition to the shortest time delay are necessary to obtain tight constraints on the inner slope α.

5. Discussion and Conclusions

We have presented predictions of time delays for the giant quadruple lensed quasar SDSS J1004+4112, and investigated the relationship between the time delays and the inner slope of the lensing cluster. We adopt a two-component model in which the brightest cluster galaxy and the cluster are described by the singular isothermal ellipsoid and the generalized NFW profile. We parameterize the inner slope of the cluster component by α such that $\rho \propto r^{-\alpha}$ in

the innermost region. The values of the slope α we have considered are 0.5, 0.75, 1.0, 1.25, and 1.5, while fixing the scale length to be $40''$. We have derived a group of mass models that fit the observables, and calculated the range of predicted time delays for each α. For observables, we have used the data of image positions, fluxes, and the position angle of the galaxy to predict the time delays. We have obtained a set of 100 acceptable models for each α, and constructed the PDFs of the predicted time delays and the ratios between them.

We have found that predicted time delays indeed depend on the inner slope, such that the steeper inner profiles (larger α) predict longer time delays. All the two of them are approximately proportional to each other, but the ratios depend slightly on the inner slope, which suggests that different α leads to a different structure of the PDFs of multiple time delays. The larger α models predict longer minimum and maximum time delays, and have longer tails at the higher end of the cumulative probabilities. The time delays Δt_{CB} and Δt_{CA} give slightly different feature in short time delay — the models with different α show almost same distributions. It is interesting that the model uncertainties resemble the inner slope uncertainty in prediction of time delays, and it would be a clue to investigate the model uncertainties.

To illustrate how well we can constrain the inner slope by adding measurements of time delays, we have calculated the likelihood function for α. Figure 8 has shown that the slope α is constrained weakly with the measurement of one time delay. However, we also found that multiple time delays will results in reasonably strong constraints ($\sigma_\alpha \lesssim 0.25$) on the inner slope. We note that we assumed observational errors of time delays to be 10%, which may be too conservative. For instance, Q 0957+561 has a time delay of ~ 420 days and the error is measured to be 1% (Kundic et al. 1997; Oscoz et al. 2001). If this level of errors can be achieved for SDSS J1004+4112, we will be able to determine the inner slope more tightly.

Our model predictions offer useful guidance for photometric monitoring of this lens system to determine the time delays. We found that 95% of models of $\alpha = 0.5 - 1.5$ have the predicted time delays of $\Delta t_{BA} \lesssim 28$, $\Delta t_{CB} \lesssim 1400$, and $\Delta t_{CD} \lesssim 3700$ in units of h_{70}^{-1} days. The first time delays is similar to those in any other lensed quasars, and therefore it can be measured easily. Indeed, the preliminary detection of the time delay between B and A has been made to be ~ 25 days (C. S. Kochanek, private communication). The second shortest time delay Δt_{CB} is $\sim 30 - 40$ times larger than Δt_{BA}, thus assuming the measured Δt_{BA} we predict $\Delta t_{CB} = 750 - 1000$ days. This is somewhat longer than observed time delays in any other systems, but is not impossible to measure. The longest time delays need monitoring more than ~ 10 years, making the measurement quite challenging.

The mass profile of the lensing cluster can be constrained much better if we combine the time delay measurements with other observations. For instance we may add constraints from multiply imaged galaxies behind the cluster (Sharon et al. 2005). The multiple arcs that have different redshifts (and therefore different Einstein ring radii) are an independent tool to constrain the cluster mass profile, especially the radial mass slope α. Other such

17

observations includes X-ray measurements of intra-cluster medium and the measurement of the velocity dispersion of the brightest cluster galaxy (eq. [8]). By combining these complementary information, we will be able to reveal the detailed distribution of the dark matter of the lensing cluster in a robust manner.

We are grateful to Takahiko Matsubara, Naohisa Inada, and Chris Kochanek for discussions.

References

Bourassa, R. R., & Kantowski, R. 1975, ApJ, 195, 13

Bourassa, R. R., & Kantowski, R. 1976, ApJ, 205, 674

Bourassa, R. R., Kantowski, R., & Norton, T. D. 1973, ApJ, 185, 747

Broadhurst, T., et al. 2005, ApJ, 621, 53

Chiba, M. 2002, ApJ, 565, 17

de Blok, W. J. G., & Bosma, A. 2002, A&A, 385, 816

Diemand, J., Moore, B., & Stadel, J. 2004, MNRAS, 353, 624

Freedman, W. L., et al. 2001, ApJ, 553, 47

Fukushige, T., & Makino, J. 1997, ApJ, 477, L9

Fukushige, T., & Makino, J. 2001, ApJ, 557, 533

Fukushige, T., & Makino, J. 2003, ApJ, 588, 674

Fukushige, T., Kawai, A., & Makino, J. 2004, ApJ, 606, 625

Gentile, G., Salucci, P., Klein, U., Vergani, D., & Kalberla, P. 2004, MNRAS, 351, 903

Ghigna, S., Moore, B., Governato, F., Lake, G., Quinn, T., & Stadel, J. 2000, ApJ, 544, 616

Hayashi, E., et al. 2004, MNRAS, 355, 794

Hennawi, J. F., Dalal, N., Bode, P., & Ostriker, J. P. 2005, ApJ, submitted (astro-ph/0506171)

Inada, N., et al. 2003, Nature, 426, 810

Inada, N., et al. 2005, PASJ, 57, L7

Jing, Y. P., & Suto, Y. 2000, ApJ, 529, L69

Kaiser, N., & Squire, G. 1993, ApJ, 404, 441

Kawano, Y., Oguri, M., Matsubara, T., & Ikeuchi, S. 2004, PASJ, 56, 253

Keeton, C. R. 2001, preprint (astro-ph/0102340)

Keeton, C. R., Kochanek, C. S., & Falco, E. E. 1998, ApJ, 509, 561

Keeton, C. R., Kochanek, C. S., & Seljak, U. 1997, ApJ, 482, 604

Keeton, C. R., & Winn, J. N. 2003, ApJ, 590, 39

Kochanek, C. S. 2002, ApJ, 578, 25

Kochanek, C. S., & Dalal, N. 2004, ApJ, 610, 69

Kochanek, C. S., Morgan, N. D., Falco, E. E., McLeod, B. A., Winn, J. N., Dembicky, J., & Ketzeback, B. 2005, ApJ, submitted (astro-ph/0508070)

Kundic, T., et al. 1997, ApJ, 482, 75

Mao, S., & Schneider, P. 1998, MNRAS, 295, 587

Moore, B., Quinn, T., Governato, F., Stadel, J., & Lake, G. 1999, MNRAS, 310, 1147

Navarro, J. F., Frenk, C. S., & White, S. D. M. 1996, ApJ, 462, 563

Navarro, J. F., Frenk, C. S., & White, S. D. M. 1997, ApJ, 490, 493

Oguri, M., et al. 2004, ApJ, 605, 78

Oguri, M., & Kawano, Y. 2003, MNRAS, 338, L25

Oguri, M., & Keeton, C. R. 2004, ApJ, 610, 663

Oguri, M., Taruya, A., Suto, Y., & Turner, E. L. 2002, ApJ, 568, 488

Oscoz, A., et al. 2001, ApJ, 552, 81

Pindor, B., et al. 2005, AJ, in press (astro-ph/0509296)

Power, C., Navarro, J. F., Jenkins, A., Frenk, C. S., White, S. D. M., Springel, V., Stadel, J., & Quinn, T. 2003, MNRAS, 338, 14

Reed, D., Governato, F., Verde, L., Gardner, J., Quinn, T., Stadel, J., Merritt, D., & Lake, G. 2005, MNRAS, 357, 82

Refsdal, S. 1964, MNRAS, 128, 307

Saha, P., & Williams, L. L. R. 1997, MNRAS, 292, 148

Salucci, P., & Burkert, A. 2000, ApJ, 537, L9

Sato, S., Akimoto, F., Furuzawa, A., Tawara, Y., Watanabe, M., & Kumai, Y. 2000, ApJ, 537, L73

Schneider, P. 2005, astro-ph/0509252

Schneider, P., Ehlers, J., & Falco, E. E. 1992, Gravitational Lenses (New York: Springer)

Sharon, K., et al. 2005, ApJ, 629, L73

Spergel, D. N., & Steinhardt P. J. 2000, Phys. Rev. Lett., 84, 3760

Spergel, D. N., et al. 2003, ApJS, 148, 175

Swaters, R. A., Madore, B. F., van den Bosch, F. C., & Balcells, M. 2003, ApJ, 583, 732

Tasitsiomi, A., Kravtsov, A. V., Gottlöber, S., & Klypin, A. A. 2004, ApJ, 607, 125

Walsh, D., Carswell, R. F., & Weymann, R. J. 1979, Nature, 279, 381

Wambsganss, J., & Paczyński, B. 1994, AJ, 108, 1156

Weinberg, M. D., & Katz, N. 2002, ApJ, 580, 627

Weymann, R. J., et al. 1980, Nature, 285, 641

Williams, L. L. R., & Saha, P. 2004, 128, 2631

Wucknitz, O. 2002, MNRAS, 332, 951

York, D. G., et al. 2000, AJ, 120, 1579

Table 3. Input Time Delays in Likelihood Analysis

Name	Δt_{BA}	Δt_{CB}	Δt_{CD}
0.5-1	9.0	281.0	929.1
0.5-2	11.4	591.3	1737.4
0.5-3	6.7	274.7	966.7
0.5-4	11.1	62.4	1783.3
0.5-5	2.0	40.0	242.3
0.5-6	14.9	661.6	2048.2
0.5-7	2.8	65.7	489.2
0.5-8	10.4	152.9	1173.0
0.5-9	14.4	248.2	1910.4
0.75-1	5.0	231.8	1151.2
0.75-2	21.1	456.3	2482.0
0.75-3	14.2	482.7	1539.8
0.75-4	13.7	659.0	2443.8
0.75-5	8.5	384.7	1435.5
0.75-6	8.7	379.1	1327.6
0.75-7	7.7	350.4	1257.7
0.75-8	15.8	602.2	2191.1
0.75-9	12.6	685.6	2293.0
1.0-1	13.7	589.2	2240.6
1.0-2	17.6	388.6	1188.9
1.0-3	22.5	1211.2	3995.2
1.0-4	7.9	254.2	1113.2
1.0-5	5.0	133.6	688.0
1.0-6	21.4	1154.7	3687.3
1.0-7	11.0	475.8	1679.8
1.0-8	9.4	391.7	1407.1
1.0-9	5.7	67.0	617.4
1.25-1	25.7	1490.8	4116.4
1.25-2	27.7	1509.39	4522.2
1.25-3	7.3	119.1	868.6
1.25-4	38.1	1190.5	4671.4
1.25-5	11.1	172.1	1815.6
1.25-6	27.4	1353.4	4567.2
1.25-7	10.8	353.2	1629.7
1.25-8	7.9	167.1	849.8

Table 3. (Continued.)

Name	Δt_{BA}	Δt_{CB}	Δt_{CD}
1.25-9	9.9	254.3	1166.2
1.5-1	18.9	872.0	2796.9
1.5-2	22.8	1157.7	3635.5
1.5-3	35.8	1877.9	5021.0
1.5-4	11.1	286.7	2000.2
1.5-5	10.8	254.6	1320.7
1.5-6	15.9	653.5	2406.9
1.5-7	9.4	133.1	1159.5
1.5-8	8.3	17.2	1311.6
1.5-9	40.0	1324.3	4331.2

* Name of data are expressed as (input α-data number).
† Time delays in units of h_{70}^{-1}. The observational errors are assumed to be 10%.